RSC Advances

PAPER

View Article Online
View Journal | View Issue

Check for updates

Cite this: *RSC Adv.*, 2018, **8**, 36616

Facile synthesis of highly conductive MoS_2/graphene nanohybrids with hetero-structures as excellent microwave absorbers†

Jixing Chai,‡[ab] Deqing Zhang,‡*[ab] Junye Cheng,[cd] Yixuan Jia,[b] Xuewei Ba,[b] Ya Gao,[e] Lei Zhu,[f] Hao Wang*[c] and Maosheng Cao *[g]

Two-dimensional (2D) MoS_2/graphene nanosheet (MoS_2/GN) hybrids have been demonstrated to be promising microwave absorption (MA) materials due to their unique chemical and physical properties as well as rich impedance matching. However, the reported strategies for preparing MoS_2/GN hybrids have limited their application potential due to the complex, high-cost and inefficient preparation processes. On the other hand, it is of note that the main source of graphene is based on converting insulating graphene oxides (GO) back to conductive reduced graphene oxides (RGO). Thus, the MA performance of obtained MoS_2/RGO nanohybrids is greatly affected by the conversion process of GO. In this work, we prepared the MoS_2/GN hybrids by a facile hydrothermal method with directly introducing highly pure and electroconductive GNs. It is found that the highest reflection loss value of the sample-wax containing 40% MoS_2/GN is −57.31 dB at a thickness of 2.58 mm, and the bandwidth of RL values less than −10 dB can reach up to 12.28 GHz (from 5.72 to 18 GHz) when an appropriate absorber thickness between 1.5 and 4 mm is chosen. The excellent MA performances emanate from effective conjugation of MoS_2 with GN (Mo–C bond between the interfaces), which provides the dielectric loss caused by multi-relaxation, conductance, and polarization. Taking into account the facile synthesis route and their excellent MA performance, the MoS_2/GNs hybrid nanosheets and those composite materials with similar isomorphic hetero-structures are very promising for a wide range of MA applications.

Received 29th September 2018
Accepted 24th October 2018

DOI: 10.1039/c8ra08086k

rsc.li/rsc-advances

1. Introduction

With more and more electronic communication devices around us, the resulting electromagnetic pollution is becoming a threat to human beings. Therefore, designing and preparing efficient microwave absorbing (MA) materials is crucial to governing electromagnetic pollution.[1–6] Two-dimensional (2D) materials, specially molybdenum disulfide (MoS_2), have attracted attention as MA materials due to their size effect, high specific surface areas and remarkable mechanical properties.[7–11] However, the further application of pure MoS_2 is limited by narrow bandwidth; low RL value and the poor impedance matching of single component materials.[12–15]

Therefore, one of the strategies is introducing a second phase, such as magnetic ferrite (Fe_3O_4),[16,17] carbon materials (CNT, GN),[18,19] and conductive polymers (PEDOT),[20,21] into/onto the matrix to improve the MA performance and enrich impedance matching.[22–24] Zhang *et al.*[25] synthesized MoS_2/Fe_3O_4 hybrids through a hydrothermal and coprecipitation method and they exhibited outstanding MA performance. Pan *et al.*[26] reported a porous coin-like Fe@MoS_2 composite which optimized impedance matching and showed efficient microwave absorption. Zhang *et al.*[27] fabricated MoS_2/PANI-NDs composites *via* an *in situ* oxidation polymerization which exhibited tunable electromagnetic wave attenuation performance. Liu *et al.*[28] prepared 3D hierarchical MoS_2 nanosheets/ultralong N-doped carbon nanotubes as a high-performance electromagnetic wave absorbing material.

Among these second phase materials, graphene shows great potential due to its exclusive structures and electrical properties. Wang *et al.*[29] first synthesized MoS_2/RGO hybrids by

---

[a] Heilongjiang Provincial Key Laboratory of Polymeric Composite Materials, Qiqihar University, Qiqihar 161006, China. E-mail: zhdqing@163.com

[b] School of Materials Science and Engineering, Qiqihar University, Qiqihar 161006, China

[c] Guangdong Provincial Key Laboratory of Micro/Nano Optomechatronics Engineering, College of Mechatronics and Control Engineering, Shenzhen University, Shenzhen 518060, China. E-mail: whao@szu.edu.cn

[d] Center of Super-Diamond and Advanced Films, Department of Materials Science and Engineering, City University of HongKong, HongKong 999077, China

[e] School of Chemistry and Chemical Engineering, Qiqihar University, Qiqihar 161006, China

[f] School of Communication and Electronic Engineering, Qiqihar University, Qiqihar 161006, China

[g] School of Materials Science and Engineering, Beijing Institute of Technology, Beijing 100081, China. E-mail: caomaosheng@bit.edu.cn

† Electronic supplementary information (ESI) available. See DOI: 10.1039/c8ra08086k

‡ These authors contributed equally to this work.

chemical vapor deposition and the highest reflection loss value is −50.9 dB. Ran *et al.*[30] reported the synthesis of MoS_2/RGO hybrids by a three-step ultrasonic method and that the highest reflection loss value was −49.7 dB. It should be noted that the preparation of MoS_2/graphene hybrids with hetero-structures involves the conversion of insulating GO into conductive RGO using reducing agents or high-temperature thermal annealing treatments.[31,32] The conversion process is usually tedious and with some troubles, such as insufficient conductivity recovery, morphological changes, phase transitions, even samples polluted with reducing agents. And the reported preparation of MoS_2/graphene hybrids with pure GNs is inefficient and high-cost, which is not viable from the viewpoint of practical application.

In this work, we develop a hydrothermal method to prepare dielectric MoS_2-nanosheets (MoS_2-NS) and MoS_2/GN hybrids with hetero-structures, using molybdic acid; thiourea to grow on pure GN (Scheme 1). This synthesis strategy for MoS_2 and MoS_2/GN hybrids could be applied in various research areas including catalysis, environmental remediation and hydrogen evolution. The as-synthesized MoS_2/GN hybrids show efficient MA performance, and we also investigate the MA performance mechanisms of MoS_2/GN hybrids.

2. Experimental

All chemicals were in analytical grade and used without further purification. Molybdic acid ($H_2MoO_4 \geq 85\%$) was purchased from Shanghai Aladdin Biochemical Technology Co. Ltd. Thiourea (CH_4N_2S) was purchased from Tianjin Fuchen Chemical Reagent Factory. Natural graphite powders were purchased from Qingdao YUBO graphite Technology Co, LTD. Deionized water was purchased from Qiqihar Tianyuan Water Supply Company.

Graphene was prepared from graphite power by a liquid-phase ultrasound method.[15] MoS_2/GN hybrids were prepared by an improved one-step hydrothermal method. Firstly, 40 mg graphene-nanosheets (GN) was dispersed in 40 mL of ethanol/deionized water mixture (volume ratio: 1/3). Secondly, 0.4 g H_2MoO_4 and 0.75 g CH_4N_2S were added into the above dispersions. After magnetic stirring for 30 min, the mixture was transferred to a 100 ml Teflon-lined autoclave with a magnetic stirring device. After heated and stirred for 10 hours at 200 °C, the mixtures were subsequently cooled down to room temperature at natural circumstances. Finally MoS_2/GN hybrids were washed with deionized water and ethanol for several times and dried at 60 °C under vacuum oven.

The morphology of samples was characterized by transmission electron microscope (TEM: Japan Hitachi H7650). The crystallization properties were investigated by an X-ray diffractometer (Bruker Company, D8) using the Cu-Kα radiation ($\lambda = 0.15418$ nm). The crystal structure of samples was further observed with high-resolution electron microscopy (HRTEM: Tecnai F30). X-ray photoelectron spectra (XPS) were recorded using a Thermo Scientific ESCALAB MK II with an Mg Kα excitation source. Raman spectroscopy measurements were performed *via* a Lab RAM HA Evolution. The complex permittivity and permeability were measured in a frequency range of 2–18 GHz with a coaxial wire method using an Agilent N5244A network analyzer.

3. Results and discussion

The XRD patterns of GN; MoS_2 and MoS_2/GN are shown in Fig. S1† and 1a. The MoS_2-nanosheets show diffraction peaks at $2\theta = 14.6°$, 32.8°, 39.8° and 58.5° corresponding to the (002), (100), (103), and (110) planes (PDF37-1492). It is worth noting that there are no diffraction peaks for GN at the patterns of MoS_2/GN hybrids, suggesting the weak scattering power and low crystallinity of very small amount of GNs added. However, the existence of GNs in the hybrid could be identified by Raman spectroscopy (Fig. 1b). There are two strong peaks located at 1345 and 1587 cm^{-1}, which correspond to the D- and G-bands for GNs. It is also observed that the weak E_{2g} and A_{1g} peaks

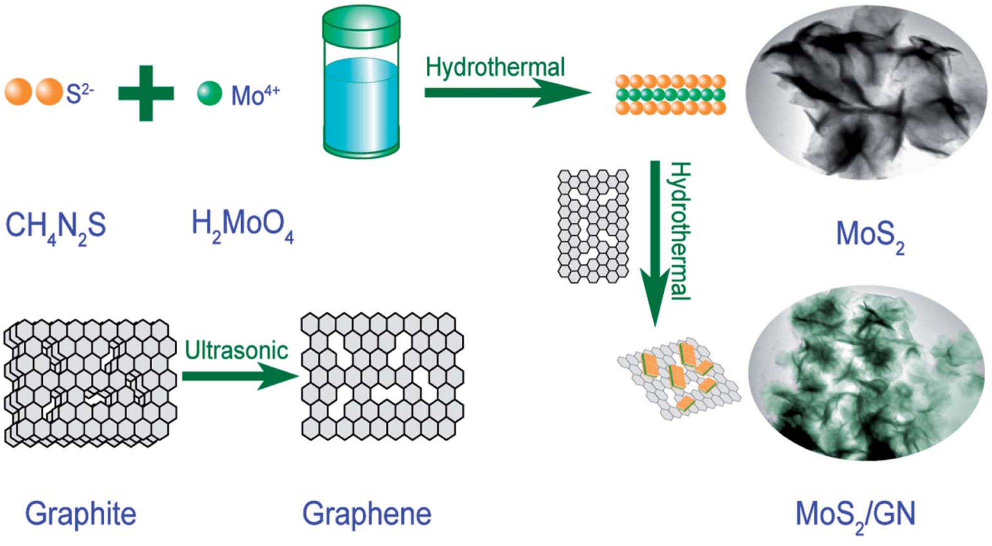

Scheme 1 Synthetic route for the MoS_2/GN hybrids.

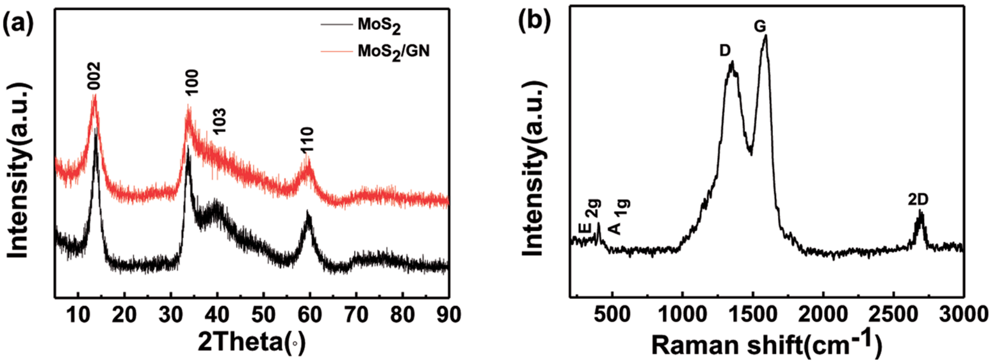

Fig. 1 (a) X-ray powder diffraction (XRD) patterns for MoS_2 and MoS_2/GN; (b) Raman spectrum for MoS_2/GN.

for MoS_2 are located at 376 and 405 cm^{-1}.[29] In general, the number of layers of graphene is usually determined by the 2D/G ratios. In this work, the 2D/G ratio of MoS_2/GN hybrids is 0.21 ($0.07 < 0.21 < 0.3$), corresponding to triple-layer graphene sheets,[33] which consistent with pure GN (as shown in Fig. S2†).

Typical morphology information of the MoS_2/GN hybrids is obtained by TEM. Fig. 2a shows that 2D MoS_2 nanosheets look like a flexible flower. The corresponding selected area electron diffraction (SAED) patterns of the MoS_2-nanosheets are also presented in the inset of Fig. 2a, two diffraction rings in the SAED patterns agree well with the (110) and (100) planes of MoS_2. Fig. 2b shows that GN looks thin and light. The overall morphology image of MoS_2/GN hybrids is shown in Fig. 2c. As presented, it can be clearly seen that the flower-like MoS_2-NS are evenly attached on the GNs. The further micromorphology information of MoS_2/GN composites is displayed by HRTEM, and the interplanar spacing of 0.62 and 0.27 nm observed in Fig. 2d are corresponding to the (002) and (100) planes of hexagonal MoS_2 crystalline structure.[22,34]

The MoS_2/GN hybrids were also characterized by X-ray photoelectron spectroscopy (XPS). As shown in Fig. 3a, there are only the Mo, S, C and O elements in the survey spectrum, and the atomic contents of Mo and S are 15.52% and 31.76%, respectively. The ratio of Mo/S is very close to 1 : 2. The Mo spectrum for MoS_2/GN as shown in Fig. 3b, the bands located at binding energies of 232.05 and 228.75 eV were assigned to the Mo ($3d_{3/2}$) and Mo ($3d_{5/2}$) in the normal state of Mo^{4+} chemical state, respectively. Moreover, the peak deconvolution of the Mo (3d)

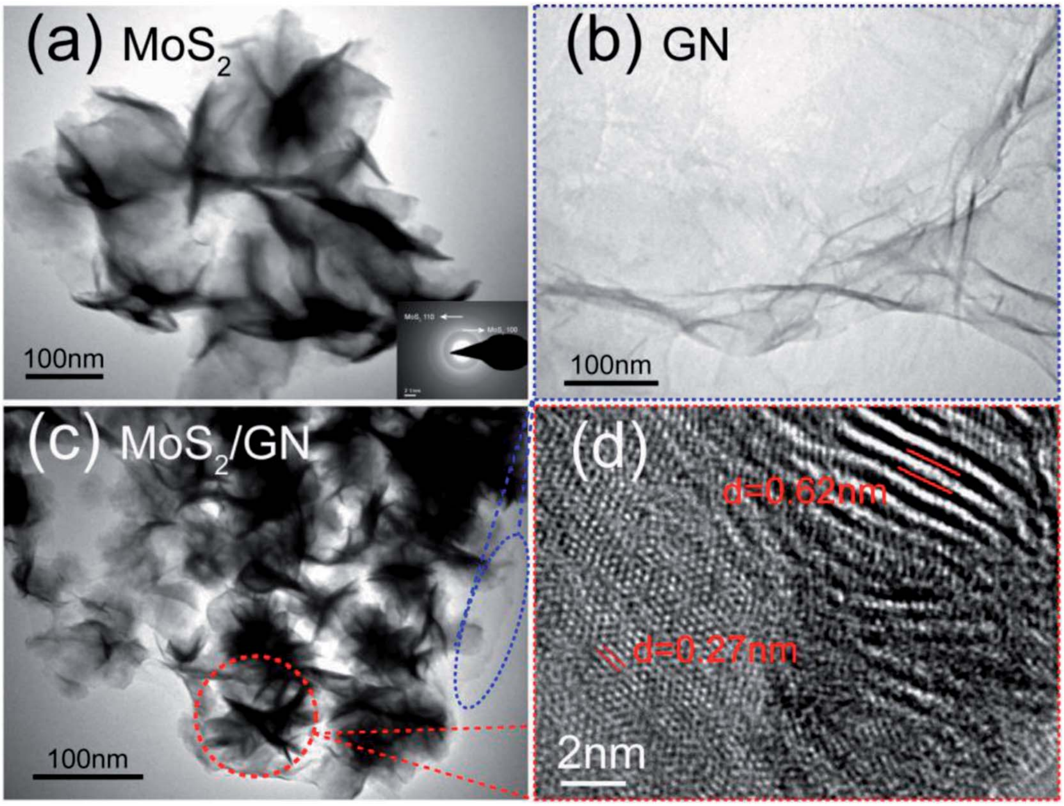

Fig. 2 TEM images of MoS_2 (a); GN (b); MoS_2/GN (c); HRTEM image of MoS_2/GN (d).

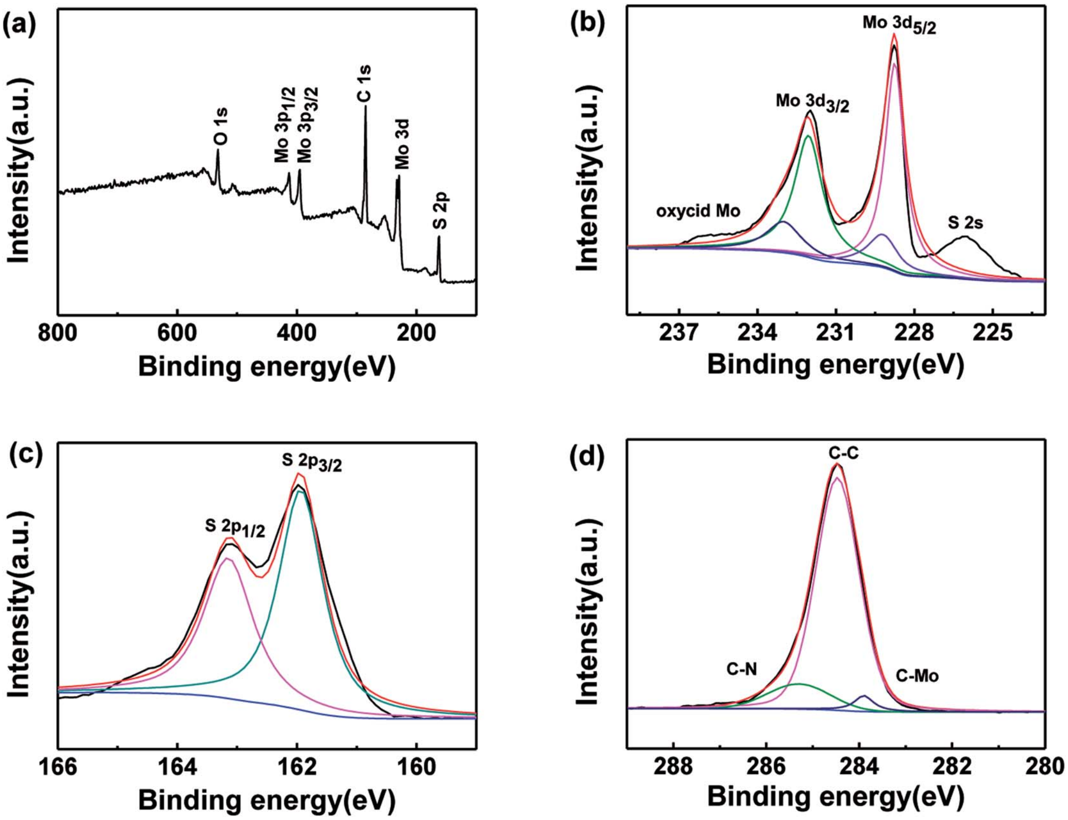

Fig. 3 XPS spectra of the MoS_2/GN samples: overall spectrum as marked (a); Mo 3d (b); S 2p (c); C 1s (d).

spectrum of the MoS_2/GN hybrids indicated two other weak peaks located at 233.00 and 229.20 eV which were attributed to formation of a Mo–C bond on the hybrids, that is, formation of MoS_2/GN hetero-structures. That shows during the prepared process some carbon diffused into the MoS_2 to substitute in the lattice of MoS_2 at the interfaces.[35–37] The S spectrum of MoS_2/GN can be observed to have two peaks located at 162.82 and 161.71 eV, as shown in Fig. 3c, in consistent with the existence of MoS_2. The C 1s spectrum can be deconvoluted into two peaks located at 285.30 and 284.47 eV (Fig. 3d), which correspond to the C–N and C–C functionalities, respectively. Moreover, the band located at 283.90 eV was assigned to the presence of the Mo–C bond, which also proved the formation of hetero-structures.

The MA performance can be evaluated by the values of reflection loss (RL) *versus* frequency which can be determined according to transmission line theory.[38–41] The RL is calculated with the following formulas:

$$R_L = 20\log\frac{|Z_{in} - Z_0|}{|Z_{in} + Z_0|} \tag{1}$$

where the normalized input impedance (Z_{in}) is given by

$$Z_{in} = \sqrt{\frac{\mu_r}{\varepsilon_r}}\tanh\left[j\frac{2\pi}{c}\sqrt{\mu_r\varepsilon_r}fd\right] \tag{2}$$

where Z_0 is the impedance of free space, c is the velocity of light, f is the frequency, and d is the thickness of the absorber. ε_r is the complex permittivity, $\varepsilon = \varepsilon' - j\varepsilon''$, μ_r is the complex permeability, $\mu = \mu' - j\mu''$.

Fig. 4 shows the RL curves of MoS_2–wax composites and MoS_2/GN–wax composites with different loading contents (from 30 to 50 wt%) in the frequency range of 2–18 GHz at the thickness of 2.5 mm. It can be found that under the same loading of 40 wt%, the value of RL for MoS_2/GN hybrid (−43.68 dB) is much larger than that of pure MoS_2 (−19.83 dB). For the MoS_2/GN-wax composites, it can be found that the MA performance of MoS_2/GN-wax composites improves with the increasing loading of MoS_2/GN from 30 to 40 wt%. Nevertheless, degraded MA performance is also observed for the sample with the MoS_2/GN loading of 50 wt%. In summary, the MoS_2/GN–wax

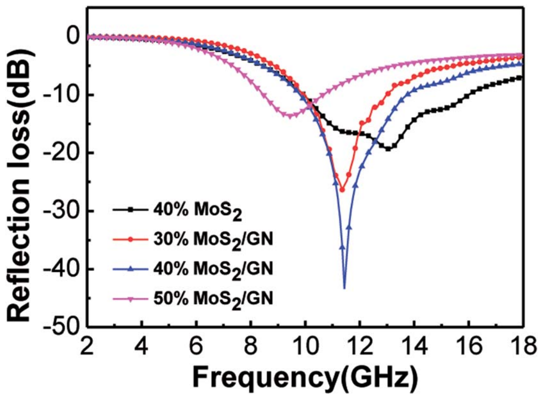

Fig. 4 RL curves of MoS_2 and MoS_2/GN composites mixed with paraffin with different loading (thickness: 2.5 mm, frequency: 2–18 GHz).

composites containing 40 wt% loading exhibited the outstanding microwave absorption properties.

Fig. 5 shows the RL value and 3D plots for MoS_2–wax composites, GN–wax composites and MoS_2/GN–wax composites with different thickness (40 wt% loading). The minimum RL is observed to be −57.31 dB at 11.03 GHz for MoS_2/GN with a thickness of 2.58 mm; the bandwidth of RL values less than −10 dB can reach up to 12.28 GHz (from 5.72 to 18 GHz) when an appropriate absorber thickness between 1.0 and 4 mm is chosen (as shown Fig. 5a). Compared with the MoS_2/GN hybrids, the MoS_2-NS and GN-NS exhibit poor MA performances (Fig. 5b and c), indicating that the combination of MoS_2 with GN is an effective method in improving the MA performance.

The permittivity and permeability of MoS_2 and MoS_2/GN with 40 wt% loadings were investigated to better understand the probable mechanism of dielectric loss or magnetic loss. Fig. 6 shows the complex permittivity; complex permeability and dielectric loss tangents ($\tan\delta_e = \varepsilon''/\varepsilon'$) of MoS_2 and MoS_2/GN hybrid in the range of 2–18 GHz. Obviously, as shown in Fig. 6a, both real (ε') and imaginary (ε'') permittivity of MoS_2/GN are found higher than that of pure MoS_2, and both real ε' and ε'' decrease with increasing frequency. As shown in Fig. 6b, the values of μ' and μ'' for both MoS_2 and MoS_2/GN are low, and are close to 1 and 0, respectively. As shown in Fig. 6c, the dielectric loss tangent of MoS_2/GN is higher than that of pure MoS_2.

In general, the change of complex permittivity can be explained according to Debye theory:[42–45]

$$\varepsilon' = \varepsilon_\infty + \frac{\varepsilon_s - \varepsilon_\infty}{1 + \omega^2\tau^2} \tag{3}$$

$$\varepsilon'' = \frac{\varepsilon_s - \varepsilon_\infty}{1 + \omega^2\tau^2}\omega\tau + \frac{\sigma}{\omega\varepsilon_0} \tag{4}$$

where ε_s, ε_∞, ω, τ, σ, and ε_0 are the static permittivity, the relative dielectric permittivity at the high frequency limit, the angular frequency, the polarization relaxation time, the electrical conductivity and the dielectric constant in vacuum, respectively.

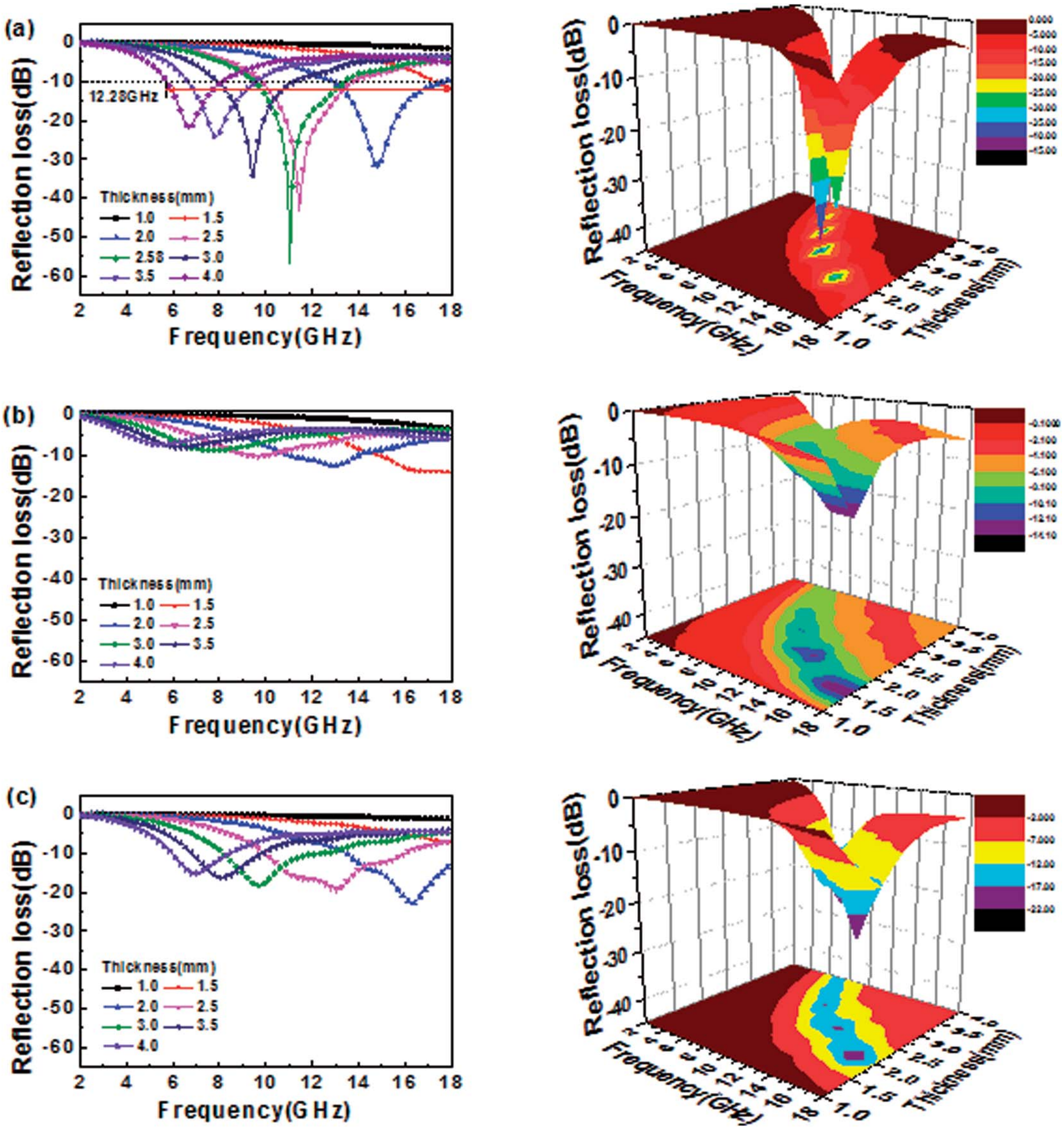

Fig. 5 RL curves and 3D plots for MoS_2/GN–wax (a); GN–wax (b); and MoS_2–wax (c) composites.

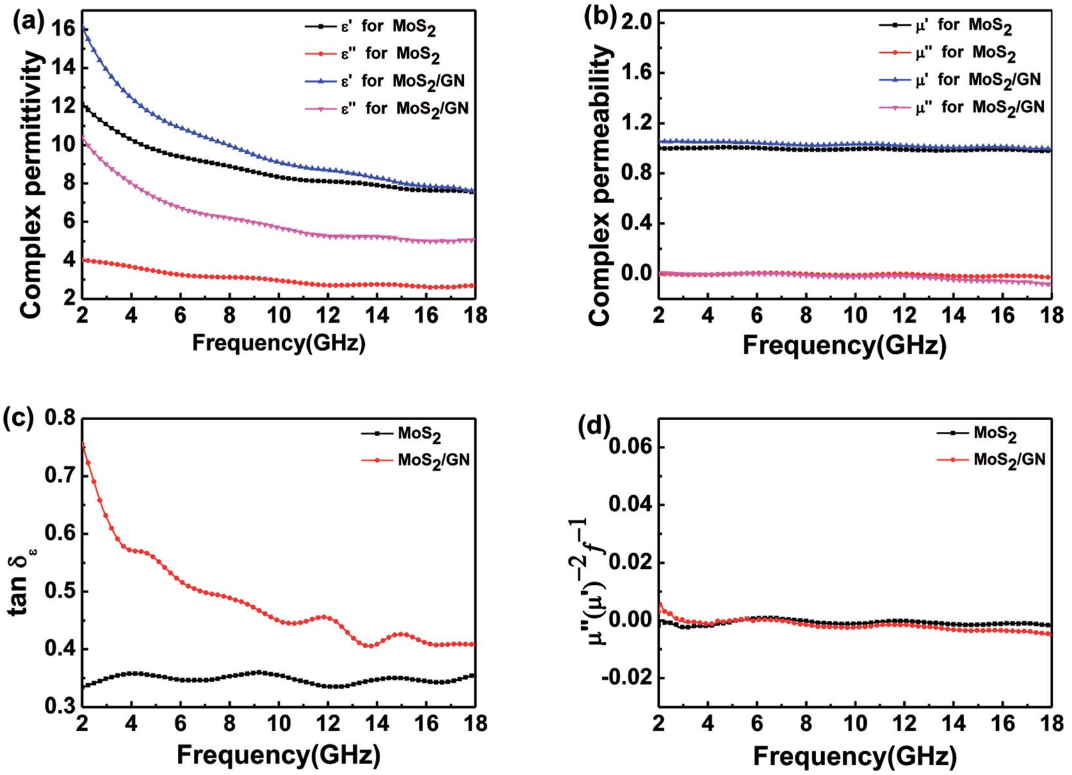

Fig. 6 The complex permittivity (a); and complex permeability (b); the dielectric loss (c) and the values of $C_0 = \mu''(\mu')^{-2}f^{-1}$ (d) in the range of 2–18 GHz for MoS_2 and MoS_2/GN composites.

According to eqn (3) and (4), the decrease in ε' and ε'' is attributed to the increase in ω. The ε' of MoS_2/GN is larger than that of MoS_2, which is due to the abundant defect polarization of GNs and interfacial polarization caused by interface coupling of MoS_2 and GNs. The electrical conductivities of the samples were measured by four probe conductivity meter. The conductivity of pure GNs and MoS_2/GN hybrids (the addition amount of GN is 10 wt%) are 27 800 S m^{-1} and 109.5 S m^{-1}, respectively. Compared to reported MoS_2/RGO composites, the conductivity of MoS_2/GN hybrids in this work is close to that of 30 wt% RGO addition amount of MoS_2/RGO hybrids (113.3 S m^{-1}) in the literature.[13] The highly conductive MoS_2/GN hybrids stem from the high electrical conductive GNs. According to the free electron theory,[14] $\varepsilon'' = 1/2\varepsilon_0\pi\rho f$, where ε_0, ρ and f are the permittivity of vacuum, the resistivity and the frequency of the electromagnetic wave, respectively. Therefore, the high electrically conductive GNs result in the enhanced ε'' values of MoS_2/GN. The μ' and μ'' for both MoS_2 and MoS_2/GN are low and no obvious changes appear due to lack of magnetic components in the composite-wax of MoS_2 and MoS_2/GNs. However, possible magnetic loss for MoS_2 and MoS_2/GN were also investigated. As shown in Fig. 6d, the value of $\mu''(\mu')^{-2}f^{-1}$ is almost a constant within the range of 4–18 GHz, indicating that the eddy current loss is the main contribution of the magnetic loss in MoS_2 and MoS_2/GN at 4.0–18.0 GHz.

As presented, the MA performance of MoS_2 and MoS_2/GN are mainly determined by dielectric loss. In order to investigate and better understand the dielectric loss, the relationship between the relative complex permittivity is expressed by the equation:

$$\left(\varepsilon' - \frac{\varepsilon_s + \varepsilon_\infty}{2}\right)^2 + (\varepsilon'')^2 = \left(\frac{\varepsilon_s + \varepsilon_\infty}{2}\right)^2 \tag{5}$$

which corresponds to a circle centered at $((\varepsilon_s + \varepsilon_\infty)/2,\ 0)$ in the spectrum, representing the Debye relaxation process. The Cole–Cole plots further demonstrate the existing of multi-relaxation in MoS_2 and MoS_2/GN samples, as shown in Fig. 7a and b. Two peaks of ε'' diverge from the ideal Cole–Cole semicircles, indicating the leakage conductance in the MoS_2 and MoS_2/GN samples. It well illustrates that both relaxation loss and conduction loss play important roles in dielectric loss.

In this work, the excellent MA performance of MoS_2/GN hybrid is ascribed to the following factors. First, as shown in Fig. 8a, the addition of GN adjusts the complex permittivity of MoS_2 nanosheets, which facilitates impedance matching. Second, the additional GN also carries abundant defects (such as imperfect carbon for GN), providing a large number of dipoles, which are very helpful for dielectric relaxation. Meanwhile, the interfacial polarization in MoS_2/GN, which is considered as the capacitor-like structure, could be effective in the adsorption of electromagnetic waves (Fig. 8b). It could be supported by the mechanism of multi-polarization reported by Cao *et al.*[46] Third, electrons can absorb energy and leap on the composite nanosheets, resulting in eddy current losses (Fig. 8c). It also could be supported by Cao's Electron-Hopping model and Conductive–Network equation.[47] Fourth, the multiple scattering also plays a significant role in electromagnetic wave attenuation as shown in Fig. 8d, the sandwiched layers could

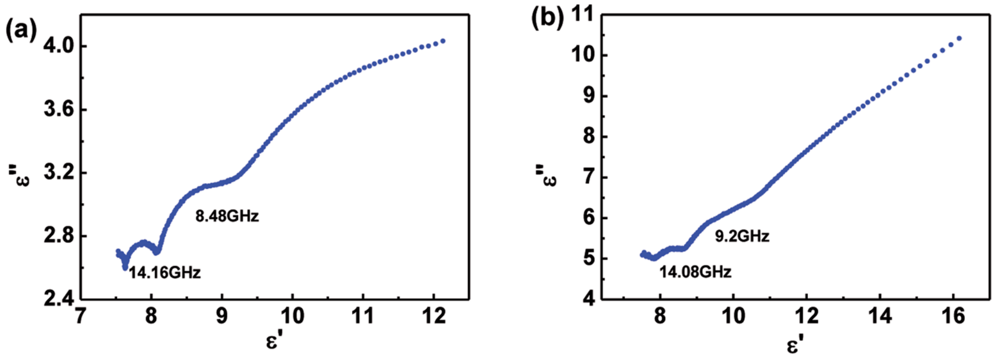

Fig. 7 The cole–cole plot of MoS_2 (a) and MoS_2/GN (b).

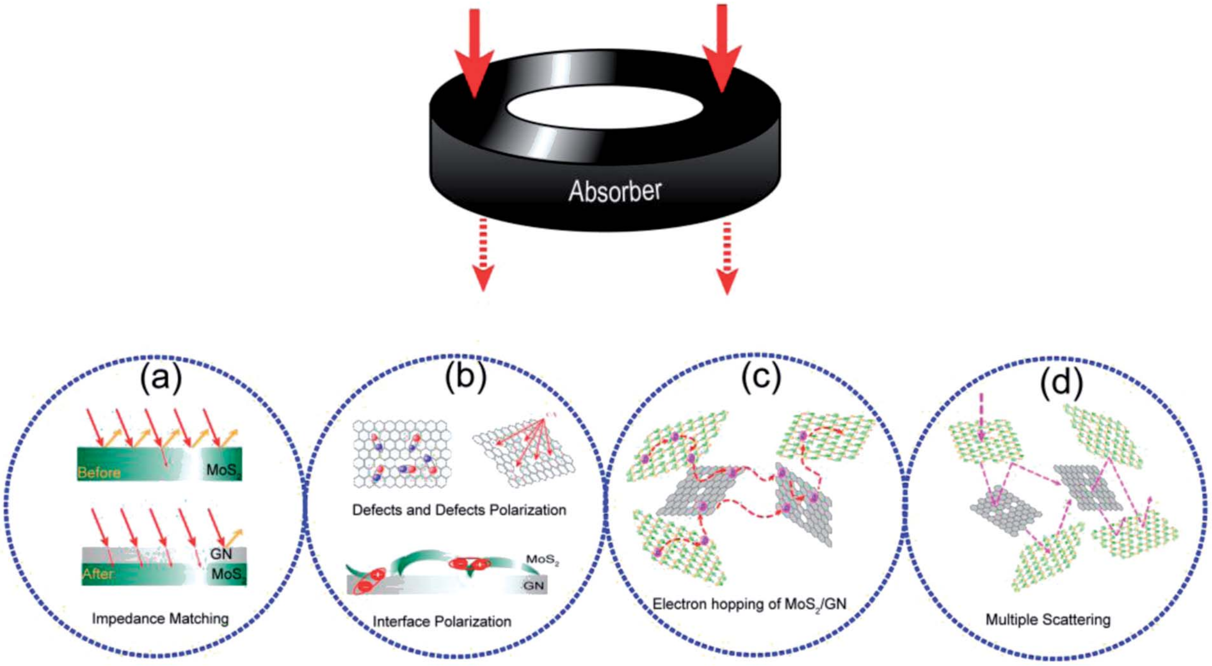

Fig. 8 (a) Impedance matching of MoS_2/GN; (b) defects and defects polarization of GN; interface polarization of MoS_2/GN; (c) electron hopping of MoS_2/GN; (d) multiple scattering of MoS_2/GN.

Table 1 Electromagnetic wave absorption performance of MA materials

	Method	Thickness (mm)	Minimum RL value (dB)	Loading ratio (wt%)	Effective bandwidth (GHz)	Ref.
MoS_2/GN	Liquid phase stripping, hydrothermal	2.58	−57.31	40	12.28	This work
MoS_2	Hydrothermal	2.0	−22.85	40	4.5	This work
MoS_2	Liquid phase stripping	2.4	−38.42	60	4.16	12
MoS_2/RGO	Hummers, chemical vapor deposition	1.9	−50.9	10	5.72	29
MoS_2/RGO	Hummers, hydrothermal	2.5	−41.53	10	5.92	13
MoS_2/RGO	Hummers, hydrothermal	2.4	−41.9	30	5.8	14
M/MoS_2/RGO	Hummers, liquid phase ultrasound	2.5	−49.7	18	5.81	30
MoS_2/GN	Liquid phase stripping, hydrothermal	2.2	−55.3	20	5.6	15

lead to the inter-layer reflection and continuous loss of electromagnetic waves. Fifth, the materials with good electrical conductivity may produce skin effect and additional reflection at the surface between materials and air,[48] which offers effective electromagnetic attenuation.

As listed in Table 1, compared with the previously reported MoS_2/graphene MA materials, the minimum RL value of MoS_2/GN hybrids in this work is higher than those of MoS_2/RGO hybrids in previous reports. Meanwhile, it is also shown that the minimum RL value of MoS_2/RGO prepared by chemical vapor deposition is higher than that of MoS_2/RGO prepared by hydrothermal method. This is because the chemical vapor deposition can help convert more insulating GO back to conductive RGO.

4. Conclusion

In summary, MoS_2 and MoS_2/GN hybrids were prepared by a facile one-step hydrothermal method, and the MoS_2-nanosheets were conjugated on the highly conductive GNs. The mechanisms of MA performance for MoS_2 and MoS_2/GN were also investigated. The excellent MA performance indicates that the MoS_2/GN hybrids with hetero-structures hold some advantages in both high conductance and high absorption performance devices. It is also believed that the simple hydrothermal method can promote the synthesis of hetero-structures nanohybrids at an industrial scale. Furthermore, the hetero-structure nanohybrids could also be readily applied in other fields.

Conflicts of interest

There is no conflict in the statement.

Acknowledgements

This work was supported by the National Natural Science Foundation of China (51272110, 51772160 and 51771123) and the Shenzhen Peacock Innovation Project (Grant No. KQJSCX20170327151307811).

References

1 W. L. Song, M. S. Cao, L. Z. Fan, M. M. Lu, Y. Li, C. Y. Wang and H. F. Ju, *Carbon*, 2014, **77**, 130–142.

2 L. L. Yan, X. X. Wang, S. C. Zhao, Y. Q. Li, Z. Gao, B. Zhang, M. S. Cao and Y. Qin, *ACS Appl. Mater. Interfaces*, 2017, **9**, 11116–11125.

3 W. L. Song, X. T. Guan, L. Z. Fan, W. Q. Cao, C. Y. Wang, Q. L. Zhao and M. S. Cao, *J. Mater. Chem. A*, 2017, **3**, 2097–2107.

4 B. Zhao, C. X. Zhao, M. Hamidinejad, C. D. Wang, R. S. Li, S. Wang, Y. Kazemi and C. B. Park, *J. Mater. Chem. C*, 2018, **6**, 10292–10300.

5 W. L. Song, X. T. Guan, L. Z. Fan, Y. B. Zhao, W. Q. Cao, C. Y. Wang and M. S. Cao, *Carbon*, 2016, **100**, 109–117.

6 S. Motojima, S. Hoshiya and Y. Hishikawa, *Carbon*, 2003, **41**, 2658–2660.

7 X. Liu, L. S. Wang, Y. T. Ma, H. F. Zheng, L. Lin, Q. F. Zhang, Y. Z. Chen, Y. L. Qiu and D. L. Peng, *ACS Appl. Mater. Interfaces*, 2017, **9**, 7601–7610.

8 X. Sun, J. P. He, G. X. Li, J. Tang, T. Wang, Y. X. Guo and H. R. Xue, *J. Mater. Chem. C*, 2012, **1**, 765–777.

9 M. S. Cao, J. Zhu, J. Yuan, T. F. Zhang, Z. H. Peng, Z. J. Guo, G. Xiao and S. M. Qin, *Mater. Des.*, 2002, **23**, 557–564.

10 M. Q. Zeng, Y. Xiao, J. X. Liu, K. N. Yang and L. Fu, *Chem. Rev.*, 2018, **118**, 6236–6296.

11 B. Zhao, L. Y. Liang, J. S. i. Deng, Z. Y. Bai, J. W. Liu, X. Q. Guo, K. Gao, W. H. Guo and R. Zhang, *CrystEngComm*, 2017, **19**, 6579–6587.

12 M. Q. Ning, M. M. Lu, J. B. Li, Z. Chen, Y. K. Dou, C. Z. Wang, F. Rehman, M. S. Cao and H. B. Jin, *Nanoscale*, 2015, **7**, 15734–15740.

13 X. Ding, Y. Huang, S. Li, N. Zhang and J. G. Wang, *Composites, Part A*, 2016, **9**, 424–432.

14 X. X. Wang, W. L. Zhang, X. Q. Ji, B. Q. Zhang, M. X. Yu, W. Zhang and J. Q. Liu, *RSC Adv.*, 2016, **6**, 106187–106193.

15 D. Q. Zhang, Y. X. Jia, J. Y. Cheng, S. M. Chen, J. X. Chai, X. Y. Yang, Z. Y. Wu, H. Wang, W. J. Zhang, Z. L. Zhao, C. Han, M. S. Cao and G. P. Zheng, *J. Alloys Compd.*, 2018, **758**, 62–71.

16 X. H. Li, H. B. Yi, J. W. Zhang, J. Feng, F. S. Li, D. S. Xue, H. L. Zhang, Y. Peng and N. J. Mellors, *J. Nanopart. Res.*, 2013, **15**, 1472.

17 G. B. Sun, B. X. Dong, M. H. Cao, B. Q. Wei and C. W. Hu, *Chem. Mater.*, 2011, **23**, 1587–1593.

18 S. Motojima, Y. Noda, S. Hoshiya and Y. Hishikawa, *J. Appl. Phys.*, 2003, **94**, 2325–2330.

19 M. Q. Ning, J. B. Li, B. Y. Kuang, C. Z. Wang, D. Z. Su, Y. J. Zhao, H. B. Jin and M. S. Cao, *Appl. Surf. Sci.*, 2018, **447**, 244–253.

20 P. B. Liu, Y. Huang and X. Zhang, *Powder Technol.*, 2015, **276**, 112–117.

21 W. C. Zhou, X. J. Hu, C. H. Sun, J. Yan, S. Y. Zhou and P. Chen, *Polym. Adv. Technol.*, 2014, **25**, 83–88.

22 M. S. Cao, J. Yang, W. L. Song, D. Q. Zhang, B. Wen, H. B. Jin, Z. L. Hou and J. Yuan, *ACS Appl. Mater. Interfaces*, 2012, **4**, 6949–6956.

23 W. Feng, Y. M. Wang, J. C. Chen, L. X. Guo, J. H. OuYang, D. C. Jia and Y. Zhou, *Phys. Chem. Chem. Phys.*, 2017, **19**, 14596–14605.

24 G. S. Wang, Y. Wu, Y. Z. Wei, X. J. Zhang, Y. Li, L. D. Li, B. Wen and M. S. Cao, *Chempluschem*, 2014, **79**, 375–381.

25 D. Q. Zhang, J. X. Chai, J. Y. Chen, Y. X. Jia, X. Y. Yang, H. Wang, Z. L. Zhao, C. Han, G. C. Shan, W. J. Zhang, G. P. Zheng and M. S. Cao, *Appl. Surf. Sci.*, 2018, **462**, 872–882.

26 J. J. Pan, X. Sun, T. Wang, Z. T. Zhu, Y. P. He, W. Xia and J. P. He, *Appl. Surf. Sci.*, 2018, **457**, 271–279.

27 W. L. Zhang, D. G. Jiang, X. X. Wang, B. N. Hao, Y. D. Liu and J. Q. Liu, *J. Phys. Chem. C*, 2017, **121**, 4989–4998.

28 L. L. Liu, S. Zhang, F. Yan, C. Y. Li, C. L. Zhu, X. T. Zhang and Y. J. Chen, *ACS Appl. Mater. Interfaces*, 2018, **10**, 14108–14115.

29 Y. F. Wang, D. L. Chen, X. Yin, P. Xu, F. Wu and M. He, *ACS Appl. Mater. Interfaces*, 2015, **7**, 26226–26234.

30 J. Ran, L. X. Shen, L. Zhong and H. Q. Fu, *Ind. Eng. Chem. Res.*, 2017, **56**, 10667–10677.

31 W. L. Song, X. T. Guan, L. Z. Fan, W. Q. Cao, C. Y. Wang and M. S. Cao, *Carbon*, 2015, **93**, 151–160.

32 X. Liang, B. Quan, G. B. Ji, W. Liu, H. W. Zaho, S. S. Dai, J. Lv and Y. W. Du, *ACS Sustainable Chem. Eng.*, 2017, **5**, 10570–10579.

33 O. Akhavan, *Carbon*, 2018, **81**, 158–166.

34 Y. Shi, Y. Zhou, D. R. Yang, W. X. Xu, C. Wang, F. B. Wang, J. J. Xu, X. H. Xia and H. Y. Chen, *J. Am. Chem. Soc.*, 2017, **139**, 15479–15485.

35 O. Akhavan, *Appl. Surf. Sci.*, 2010, **257**, 1724–1728.

36 O. Akhavan and E. Ghaderi, *J. Phys. Chem. C*, 2009, **113**, 20214–20220.

37 X. W. Zhang and L. C. Lei, *Appl. Surf. Sci.*, 2008, **254**, 2406–2412.

38 X. B. Li, S. W. Yang, J. Sun, P. He, X. P. Pu and G. Q. Ding, *Synth. Met.*, 2014, **194**, 52–58.

39 Y. H. Chen, Z. H. Huang, M. M. Lu, W. Q. Cao, J. Yuan, D. Q. Zhang and M. S. Cao, *J. Mater. Chem. A*, 2015, **3**, 12621–12625.

40 B. Zhao, J. W. Liu, X. Q. Guo, W. Y. Zhao, L. Y. Liang, C. Ma and R. Zhang, *Phys. Chem. Chem. Phys.*, 2017, **19**, 9128–9136.

41 B. Zhao, X. Q. Guo, Y. Y. Zhou, T. T. Su, C. Ma and R. Zhang, *CrystEngComm*, 2017, **19**, 2178–2186.

42 C. L. Zhu, M. L. Zhang, Y. J. Qiao, G. Xiao, F. Zhang and Y. J. Chen, *J. Phys. Chem. C*, 2010, **114**, 16229–16235.

43 B. Zhao, X. Q. Guo, W. Y. Zhao, J. S. Deng, B. B. Fan, G. Shao, Z. Y. Bai and R. Zhang, *Nano Res.*, 2017, **1**, 331–343.

44 B. Zhao, X. Q. Guo, W. Y. Zhao, J. S. Deng, G. Shao, B. B. Fan, Z. Y. Bai and R. Zhang, *ACS Appl. Mater. Interfaces*, 2016, **8**, 28917–28925.

45 B. Zhao, W. Y. Zhao, G. Shao, B. B. Fan and R. Zhang, *ACS Appl. Mater. Interfaces*, 2015, **7**, 12951–12960.

46 W. L. Song, X. T. Guan, L. Z. Fan, W. Q. Cao, Q. L. Zhao, C. Y. Wang and M. S. Cao, *Mater. Res. Bull.*, 2015, **72**, 316–323.

47 Y. L. Zhang, X. X. Wang and M. S. Cao, *Nano Res.*, 2017, **11**, 1426–1436.

48 X. X. Wang, T. Ma, J. C. Shu and M. S. Cao, *Chem. Eng. J.*, 2018, **332**, 321–330.